

# The Dynamics of Saturn's E Ring Particles

MIHALY HORANYI

*Lunar and Planetary Laboratory, University of Arizona, Tucson, Arizona 85721*

JOSEPH A. BURNS

*Lunar and Planetary Laboratory, University of Arizona, Tucson, Arizona 85721 and Departments of Theoretical and Applied Mechanics, and Astronomy, Cornell University, Ithaca, New York 14853*

AND

DOUGLAS P. HAMILTON

*Department of Astronomy, Cornell University, Ithaca, New York 14853*

Received July 30, 1991; revised March 27, 1992

THIS PAPER IS DEDICATED TO THE MEMORY OF CHRISTOPH K. GOERTZ, WHO CONTRIBUTED MUCH TO OUR CURRENT UNDERSTANDING OF DUSTY PLASMAS

---

Saturn's tenuous E ring, located between 3 and 8 Saturnian radii ( $R_S$ ), peaks sharply near Enceladus' orbit ( $3.95 R_S$ ) and has recently been found to be composed predominantly of grains 1 micrometer in radius. We study analytically and numerically the motion of such grains launched from Enceladus as they evolve under the action of Saturn's oblate gravity field, solar radiation pressure, and electromagnetic forces. The latter arise because grains are charged (usually to negative values) and also orbit through a dipolar magnetic field. In the absence of planetary shadowing, solar radiation pressure cannot change an orbit's semimajor axis, but it can produce periodic changes in orbital eccentricity that vary at the orbital precession rate. The orbital precession rates caused by the planetary oblateness and the Lorentz force on grains of  $1 \mu\text{m}$  radius are shown to be approximately equal in magnitude but opposite in sign at Enceladus' distance. The near-equality of these precessions for micrometer-sized grains introduced at Enceladus allows very large orbital eccentricities and correspondingly large radial excursions to develop in just a few years. Although particles on eccentric orbits are preferentially found at apocenter, the area covered by an annulus of width  $\Delta r$  is smallest at pericenter; these two effects combine such that the normal optical depth distribution is radially symmetric about the source. Owing to the long time spent at small eccentricities, however, particles injected at Enceladus are most commonly located near its orbit. In addition, solar radiation has a time-dependent component out of the ring plane arising from Saturn's obliquity and motion about the Sun. This force will cause orbital inclinations to develop and is most effective when particles are on highly eccentric orbits. Furthermore, the out-of-plane com-

ponent of radiation pressure causes the orbital nodes to lock at radial distances similar to that of the source, hence the greatest ring thickness occurs furthest from the planet while the ring is thinnest near the source. By plotting the position of a single particle over time, we show the distribution of  $1\text{-}\mu\text{m}$  grains that are injected at Enceladus and move swiftly under the above forces; this distribution has many of the characteristics of the observed E ring. Finally, we note that particles with slightly different sizes attain much smaller eccentricities since the gravitational and electromagnetic contributions to the pericenter precession rate do not cancel nearly as well. © 1992 Academic Press, Inc.

---

## INTRODUCTION

It is important to understand the dynamics of the very faint rings surrounding the giant planets since, owing to the rarity of collisions in these tenuous rings, such entities offer an excellent opportunity to learn the fundamental processes affecting the motion of individual ring particles. Because the particles comprising the ethereal rings are usually small, however, the orbital evolution of even a single particle can be quite complex: in addition to the usual gravitational perturbations (e.g., due to planetary oblateness and embedded satellites), small grains are also subject to a light pressure force which is variable (due to the planet's obliquity and its orbital motion), electromag-

netic forces, plasma and neutral drags, as well as resonant and stochastic charge variations (Burns 1992). All these processes are active to some extent in the dense rings as well, but they are obscured by other perturbations, especially collisions and collective effects.

Perhaps the best studied of all the ethereal rings is Saturn's E ring. Much of the interest in this three-dimensional structure arises because the Cassini spacecraft will make many passes through this region. Recently, Showalter *et al.* (1991) have combined spectrophotometric data of the E ring from ground-based measurements with those from the Pioneer 11 and Voyager encounters. Their most important findings are: the ring extends from  $\approx 3$  to  $\approx 8R_S$  (the radius of Saturn,  $R_S = 60,330$  km); its optical depth profile peaks sharply near the orbit of Enceladus ( $R_E = 3.95R_S$ ), making this satellite the suspected source of the ring, with a simple power law decay that is sharper inward [ $\tau \sim (r/R_E)^{15}$ ] than outward ( $\tau \sim (R_E/r)^7$ ) of Enceladus' orbit; in general, the ring shows a gradual increase in vertical thickness with distance from Saturn, ranging from  $\approx 6000$  km at its inner boundary to  $\approx 40,000$  km at its outer edges but has a local minimum at the orbit of Enceladus, where the thickness is only  $\approx 4000$  km; and, perhaps most puzzling of all, the size distribution of the particles is very narrow, being composed mainly of particles with  $1(\pm 0.3)$   $\mu\text{m}$  radii (see the Discussion section).

In the present paper we suggest that many of these observations can be understood in terms of the short-term dynamics of single particles injected at Enceladus. We demonstrate that, to some degree, the E ring's optical depth profile results from the competing effects of the perturbations due to planetary oblateness and Lorentz force, which allow the solar radiation pressure to induce quite large eccentricities for a selected particle size range including the micrometer-sized grains thought to be dominant in the ring. It may be that the narrow particle size distribution itself is also, perhaps indirectly, a consequence of these dynamics. For uncharged particles, solar radiation acting on circumplanetary micrometer-sized grains produces eccentric orbits whose nodes precess due to planetary oblateness. Because generally this precession is fairly rapid, radiation pressure is only able to force swiftly varying small-amplitude eccentricity oscillations. But when the precession due to oblateness is counteracted by that due to the Lorentz force, the eccentricity variations are much slower which allows much larger perturbations to build up. This mechanism is capable of spreading material quite quickly across large radial distances from Saturn and of producing a sharply peaked optical depth profile; its effectiveness is found to be strongly size-dependent, which is consistent with the E ring's very narrow particle size distribution.

We demonstrate this novel mechanism first with approximate analytical solutions to the orbit-averaged per-

turbation equations assuming a constant electrical charge, small eccentricities, and zero inclinations. Then we present full three-dimensional results from a detailed computer simulation in which the equations of motion were directly integrated simultaneously with the current balance expression that determines the history of the particle's charge. In these simulations we have also included the apparent motion of the Sun which, because of Saturn's obliquity, induces small inclinations; this effect appears to play a major role in explaining the ring's observed vertical profile. Our solution to this point, in contradiction to the E ring itself, has an optical depth that is symmetric about Enceladus' orbit and fails to account for material found beyond about  $6.5R_S$ ; we discuss several unmodeled effects that may eliminate these failings. Finally, we conclude by considering some possibly observable consequences predicted by our dynamical model.

### EQUATION OF MOTION; PARTICLE CHARGE

A charged dust grain (mass  $m$ , radius  $r_g$ , and charge  $Q$ ), which is orbiting a planet and is exposed to solar radiation, has an equation of motion (as written in Gaussian units in an inertial coordinate system fixed to the planet's center) of

$$\ddot{\mathbf{r}} = -\frac{\mu}{r^3} \left( 1 - \frac{1}{2} J_2 \left( \frac{R_S}{r} \right)^2 (3 \sin^2 \delta - 1) \right) \mathbf{r} + \frac{Q}{m} \left( \dot{\mathbf{r}} \times \mathbf{B} + \mathbf{E} \right) + \frac{3\mathbf{J}_0 Q_{pr}}{4\rho c d_s^2 r_g}, \quad (1)$$

where  $\mathbf{r}$  is the grain's position vector and an overdot signifies differentiation with respect to time. The first term on the right is the gravitational acceleration where  $\mu$  equals the gravitational constant ( $G = 6.668 \times 10^{-8} \text{ g}^{-1} \text{ sec}^{-2} \text{ cm}^3$ ) times Saturn's mass ( $M_S \approx 5.688 \times 10^{29} \text{ g}$ ); the planet is considered to be oblate (with  $J_2 = 0.01667$ ) and  $\delta$  is the grain's declination measured from the equatorial (ring) plane. The second term on the right is the Lorentz acceleration where  $c$  is the speed of light,  $\mathbf{B}$  is the local magnetic field, and, assuming a rigidly corotating magnetosphere,  $\mathbf{E} = (\mathbf{r} \times \boldsymbol{\Omega}) \times \mathbf{B}/c$  is the corotational electric field, with Saturn's rotation rate  $\Omega = 1.69 \times 10^{-4} \text{ sec}^{-1}$ . The last term is the acceleration due to solar radiation:  $\mathbf{J}_0 = 1.36 \times 10^6 \text{ ergs cm}^{-2} \text{ sec}^{-1}$  (pointing outward from the Sun) is the solar radiation energy flux at 1 AU,  $Q_{pr}$  is the radiation pressure coefficient (which, assuming dielectric grains, is  $\approx 1$  for  $1\text{-}\mu\text{m}$ - and  $\approx 0.3$  for  $0.1\text{-}\mu\text{m}$ -radii grains (Burns *et al.* 1979),  $\rho = 1 \text{ g cm}^{-3}$  is the grain's density, and finally  $d_s = 9.58 \text{ AU}$  is the distance of Saturn from the Sun. Plasma and neutral drags are neglected since the orbital changes due to these have very long characteristic time scales,  $T_c \approx 10^5$  years (Burns *et*

al. 1984). We also ignore mutual collisions because the E ring's optical depth of  $\approx 10^{-5}$  (Showalter *et al.* 1991) indicates that particles rarely collide.

To follow the trajectory of a dust grain self-consistently, the equation of motion (1) must be simultaneously integrated with the current balance equation, which determines the history of the grain's charge,

$$\frac{dQ}{dt} = \sum_i I_i, \quad (2)$$

where  $I_i$  represents the various charging currents, all functions of the local plasma composition, density, temperature, and radiation field;  $I_i$  also depends on the previous charging history and the velocity of the grain relative to the mean plasma flow. The plasma parameters in Saturn's inner magnetosphere are relatively well known from the Pioneer and Voyager plasma science experiments which have determined the densities and temperatures of "hot" and "cold" electron, proton, and oxygen populations (Richardson and Sittler 1990). In calculating the charge we have considered the thermal fluxes of all species, photoemission, and secondary electron emissions, using Whipple's (1981) expressions for the charging currents; a similar routine has been applied to cometary environments (Horanyi and Mendis 1987), to the Earth's magnetosphere (Horanyi *et al.* 1988), and to planetary magnetospheres (Burns and Schaffer 1989, Schaffer and Burns 1992). For the secondary electron emission parameters we choose the maximum yield  $0 \leq \delta_M \leq 2$  and the optimum energy (i.e., the incident energy at which the yield is maximum)  $E_M = 500$  eV (Draine and Salpeter 1979; cf. Willis *et al.* 1973, Suszcynsky *et al.* 1992).

When the Debye length is much less than the typical interparticle spacing, as is the case in the Richardson and Sittler (1990) model, a grain's charge can be related to its potential  $\Phi$  by

$$\Phi \approx 300 Q/r_g; \quad (3)$$

for reference a  $-1$  V surface potential on a  $1\text{-}\mu\text{m}$ -radius grain means  $\approx 700$  extra electrons on its surface. Figure 1 shows the grain's potential  $\Phi$  within the region of the E ring; this equilibrium potential is independent of  $r_g$ . Near Enceladus' orbit we find that  $-8 \leq \Phi \leq -4$  V.

#### APPROXIMATE ANALYTICAL THEORY FOR THE PLANAR CASE

In order to lay groundwork for our later, more complete numerical integrations, we first address analytically a much simpler problem. We follow the orbital evolution of a grain, having a constant charge, that is perturbed by planetary oblateness, solar radiation pressure, and the

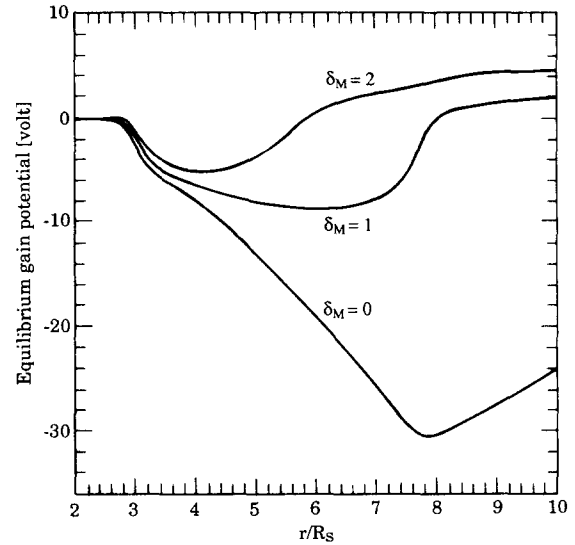


FIG. 1. The equilibrium grain potential  $\Phi$  is plotted as a function of radial distance from Saturn for grains that are kept on circular Keplerian orbits, ignoring all perturbations. The labels show three assumed values for the secondary electron emission parameter  $\delta_M$ . The observed radial dependence primarily reflects radial variations in the assumed plasma environment such as the modeled absence of significant plasma at  $\leq 3R_s$  (Richardson and Sittler 1990); the radial dependence of the difference between the local corotational and Keplerian velocities is much less important.

Lorentz force; at this point we ignore the planet's motion about the Sun and the planetary shadow. Since here we consider zero inclination ( $i = 0$ ) orbits and are only interested in the shape of the trajectory, three osculating orbital elements describe the orbital path (Danby 1988):  $a$  is the orbit's semimajor axis,  $e$  is its eccentricity, and  $\tilde{\omega}$  is the longitude of pericenter or the angle measured from the Sun's direction counterclockwise (as viewed from the North celestial pole) to pericenter. For small eccentricities ( $e \ll 1$ ), the perturbation equations for the time histories of these elements (Burns *et al.* 1979, Chamberlain 1979) can be simplified as (Horanyi *et al.* 1990)

$$\left\langle \frac{da}{dt} \right\rangle = 0 \quad (4a)$$

$$\left\langle \frac{de}{dt} \right\rangle = \beta \sin \tilde{\omega} \quad (4b)$$

$$\left\langle \frac{d\tilde{\omega}}{dt} \right\rangle = \frac{\beta}{e} \cos \tilde{\omega} + \gamma, \quad (4c)$$

where the  $\langle \rangle$  indicate orbit averaging and the quantity  $\beta \equiv \frac{3}{2} h f l \mu$  with  $h = (\mu a(1 - e^2))^{1/2}$  and  $f$  the specific (i.e., per unit mass) angular momentum and the acceleration

due to solar radiation pressure, respectively. As described directly below, the parameter  $\gamma$  represents the uniform rate at which the oblateness and the Lorentz force together would move pericenter in the absence of radiation pressure. Note that we could easily include the solar motion in  $\gamma$  as long as we continue to measure  $\dot{\omega}$  from the Sun's position; the effects of shadowing, however, are not considered since they are more difficult to represent analytically. Equation (4a) indicates that the orbit size does not change, which results from all the assumed forces being conservative ones.

In order to evaluate  $\gamma$ , we recall that a planet's oblateness causes the longitude of pericenter to precess at the rate

$$\dot{\omega}_{J_2} = \frac{3}{2} \omega_k J_2 \left( \frac{R_S}{a} \right)^2 \approx 51.4 \left( \frac{R_S}{a} \right)^{3.5} \text{ deg/day}; \quad (5)$$

the middle term is the general expression for precession under oblateness (Danby 1988) written in terms of the Keplerian angular velocity  $\omega_k^2 \equiv \mu a^{-3}$ , while the right-hand term evaluates this expression to give  $\dot{\omega}_{J_2}$  for orbits about Saturn. The Lorentz force, which is experienced when an electrically charged grain moves through the assumed corotational field, causes the pericenter to precess owing to the radial dependence of the force's strength. The precession rate for a low-eccentricity, low-inclination orbit about Saturn is

$$\begin{aligned} \dot{\omega}_\Phi &= -2 \frac{QB_0}{mc} \left( \frac{R_S}{a} \right)^3 \\ &\approx 5.1 \left( \frac{R_S}{a} \right)^3 \left( \frac{\Phi}{1 \text{ V}} \right) \left( \frac{1 \mu\text{m}}{r_g} \right)^2 \text{ deg/day}, \end{aligned} \quad (6)$$

where the central term gives the general expression (Horanyi and Burns 1991) and the right-hand term evaluates this expression, with  $Q$  given in terms of the surface potential as described in Eq. (3) and  $B_0 = -0.2 \text{ G}$  for the magnetic field strength at Saturn's surface ( $B_0$  is negative since the field evaluated at the equator is in the antispin direction).

By definition  $\gamma \equiv \dot{\omega}_{J_2} + \dot{\omega}_\Phi$ , and, since  $\Phi$  is expected to be negative (see Fig. 1), the two precessions (5) and (6) compete against one another: thus, compared to the unchanged case, the pericenter's motion can be slowed down (with  $\gamma$  remaining  $>0$ ), stopped ( $\gamma = 0$ ), or even reversed ( $\gamma < 0$ ). Which of these situations occurs will depend on the particle's size, charge, and its position in the magnetosphere.

Let us start our discussion of the solution to Eq. (4) by considering the special case where the precession rates due to oblateness and electromagnetic forces nearly can-

cel ( $\gamma \approx 0$ ). To produce this state for a grain with nominal parameters ( $r_g = 1 \mu\text{m}$ ,  $\rho = 1 \text{ g cm}^{-3}$ ,  $\beta = 0.2 \text{ year}^{-1}$ ),  $\Phi$  must be  $\approx -5 \text{ V}$ ; note that this is close to values *actually expected* throughout the region of interest for  $\delta_M = 1.5$  (see Fig. 1). In connection with initial conditions, presuming the E ring particles originate on Enceladus, we make three observations: (i) the escape velocity from the satellite is probably less than  $10^{-2}$  times the satellite's orbital velocity; (ii) electromagnetic perturbations alone do not introduce large orbital velocity changes (Schaffer and Burns 1987); and (iii) Enceladus' orbit is nearly circular. Accordingly we assume that the grain is launched at  $3.95R_S$  onto an approximately circular Keplerian orbit. From such a starting condition ( $e \sim 0$ ), Eq. (4c) shows that  $\dot{\omega}$  will swiftly turn to  $\pi/2$  and then will stay locked; simultaneously, by (4b), the eccentricity grows at the constant rate  $\beta$  (Horanyi *et al.* 1990). Of course the eccentricity can only increase until the orbit intersects the outer edge of the A ring at  $2.27R_S$  where collisions with the opaque ring will eliminate the particle; written in terms of orbital eccentricity, this condition is  $e_{\text{coll}} \approx 0.43$ . (Naturally, this applies only to particles staying in the equatorial plane whereas below we find that collisions with the main rings are less likely once the inclination is allowed to be nonzero). According to (4b)'s solution, such an eccentricity will be achieved in a little more than 2 years. To summarize, one-micrometer particles injected at Enceladus, with  $\Phi \approx -5 \text{ V}$ , will be rapidly dispersed owing to their eccentric orbits and then will be lost by collisions with the ring. We must recall, however, that it is the fine balance between the perturbations due to oblateness and the Lorentz force that anchors the pericenter in this case and allows the solar radiation pressure to induce these large eccentricities.

For the general case, where  $\gamma \neq 0$ , one can most readily solve (4b) and (4c) by transforming to the variables  $p \equiv e \sin \tilde{\omega}$  and  $q \equiv e \cos \tilde{\omega}$ , which are found to describe simple harmonic oscillations. In terms of the original variables, the solution is

$$e = \frac{2\beta}{\gamma} \left| \sin \left( \frac{\gamma}{2} t \right) \right| \quad (7a)$$

$$\tilde{\omega} = \text{modulo} \left( \frac{\gamma}{2} t, \pi \right) + \frac{\pi}{2}, \quad (7b)$$

assuming the initial condition  $e(t=0) = 0$ . The eccentricity changes periodically as the pericenter moves at a constant rate from  $\pi/2$  to  $3\pi/2$  (for  $\gamma > 0$ ), at which point  $\tilde{\omega}$  jumps back to  $\pi/2$  again (for a geometrical representation of this solution, see Horanyi and Burns 1991). The period of this solution is  $P = 2\pi/\gamma$  and the maximum eccentricity (within the approximation of small  $e$ ) is  $e_{\text{max}} = 2\beta/\gamma$ .

As seen in Eq. (6), the value of  $\gamma$ , and in turn the largest eccentricity from (7a), is sensitive to the grain size. For a specific particle size, one can compute the range of voltages that will produce precession rates such that  $e_{\text{coll}}$  is achieved. Larger voltages cause the Lorentz precession rate to dominate that from the planet's oblateness, while for smaller voltages the converse holds; both cases mitigate the ability of the solar radiation pressure to produce high eccentricities. Figure 2 displays the maximum eccentricity  $e_{\text{max}}$  achieved by particles of three sizes and various voltages near those of the nominal E ring grains. Particles on 2-D orbits are lost to the main rings when the pericenter dips into the A ring, which occurs for  $e_{\text{coll}} = 0.43$ . As we see below, three-dimensional orbits survive until the *orbital nodes* intersect the A ring (this always happens before the orbit intersects the planet) which occurs for  $e'_{\text{coll}} = 0.65$ . The curves to the left (right) of the flat tops in Fig. 2 correspond to  $\gamma < 0$  ( $> 0$ ). Because particles of different sizes are spread in such dramatically different ways, the population of grains that is present at the outskirts of the E ring could differ considerably from that introduced at Enceladus.

An excellent test of our model can be made by the Cassini spacecraft which will carry out complete photometric observations of the E ring and will thereby determine particle size distributions across the ring. Indeed, the importance of radiation pressure will be shown if a wide distribution of particle sizes is found to be present near the orbit of Enceladus but only a very selected size range is seen elsewhere. A more direct test involves using

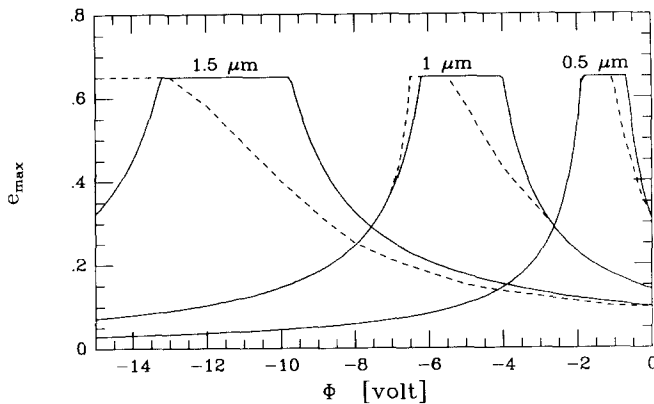


FIG. 2. The maximum eccentricity  $e_{\text{max}} = 2\beta/\gamma$  that is achieved according to (7a), as a function of the assumed (constant) surface potential for various size grains (heavy lines) introduced at Enceladus (at  $3.95R_S$ ). The results from the numerical integration of Eq. (1) are also shown (dashed lines); the differences between the curves at large eccentricities clearly signal the breakdown of the assumption in Eq. (4) that  $e \ll 1$ . The curves are truncated at  $e'_{\text{coll}} = 0.65$ , the eccentricity at which three-dimensional orbits with  $a = 3.95 R_S$  must intersect Saturn's A ring; particles confined to the ring plane will be lost once they reach  $e_{\text{coll}} = 0.43$  when the orbital pericenter dips into the outer A ring.

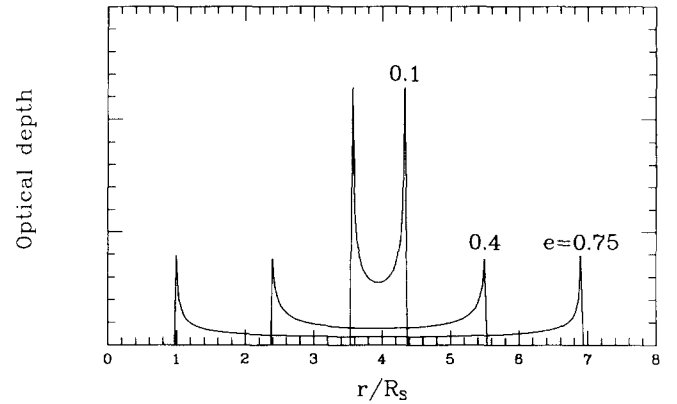


FIG. 3. The profile of optical depth vs radius plotted for grains with orbits of semimajor axis  $= 3.95R_S$  and various eccentricities. The curves, which are undefined at each orbit's pericenter and apocenter, are truncated there for clarity. The reason for the symmetry about  $3.95R_S$  is discussed in the text.

Cassini's dust detector to see whether the particles sensed at distances from Enceladus are on eccentric orbits (O. Havnes, private communication, 1991).

We now compute the radial optical depth distribution due to grains moving on elliptical orbits. For diffuse structures like the E ring, the optical depth is proportional to the time a grain spends within any given radial interval,  $r$  to  $r + \Delta r$ , which in turn is proportional to  $1/rv_r$ , where  $v_r$  is the average radial velocity over the interval considered; the extra  $r$  in the denominator appears because the area of an annulus of width  $\Delta r$  over which these particles are spread is  $2\pi r\Delta r$ . In terms of the orbital elements the radial velocity can be written as

$$v_r(r) = \left(\frac{\mu}{a}\right)^{1/2} \frac{[a^2e^2 - (r-a)^2]^{1/2}}{r}. \quad (8)$$

The radial optical depth profile due to a single particle moving along a Keplerian orbit of a given eccentricity is then

$$\tau^e(r) = \frac{T_0}{[a^2e^2 - (r-a)^2]^{1/2}}, \quad (9)$$

where  $T_0$  is a normalization constant; clearly this is valid only for distances between the orbit's radial turning points [i.e., for  $a(1-e) \leq r \leq a(1+e)$ ], elsewhere  $\tau^e(r) = 0$ . Figure 3 plots Eq. (9) for several eccentric orbits; note the symmetry about  $r = a$  and the enhanced optical depth at the orbital turning points.

A particle evolving under radiation pressure does not have a constant orbital eccentricity as assumed immediately above, but by combining Eqs. (7a) and (9), and

integrating over a full cycle of the eccentricity variation, we find that a single particle contributes to  $\tau$  as

$$\tau(r) = T_1 \int_0^{2\pi/\gamma} \tau^e(r) dt, \quad (10)$$

where  $T_1$  is another normalization constant.

Equation (10) describes a distribution sharply peaked at the radial distance of the source itself (Fig. 4). This occurs because the particle (i) spends substantial time at low eccentricity, and (ii) even when at higher  $e$ , always passes twice through its initial radius on each orbit. We note that the optical depth distributions in Figs. 3 and 4 are each symmetric about the source's orbit despite the fact that each particle spends more time at apocenter of its orbit than at pericenter; this possibly counterintuitive result arises because the apocenter particles are spread over a proportionally larger annulus. We discuss mechanisms that may introduce the observed asymmetry in Saturn's E ring after discussing our numerical results.

#### NUMERICAL RESULTS

We have numerically integrated the equation of motion (1) simultaneously with the current balance equation (2), also including Saturn's orbital motion. Due to Saturn's obliquity ( $27^\circ$ ), the solar radiation pressure introduces perturbations that lie out of the ring plane, and hence can produce orbital inclination. We use a variable step-size,

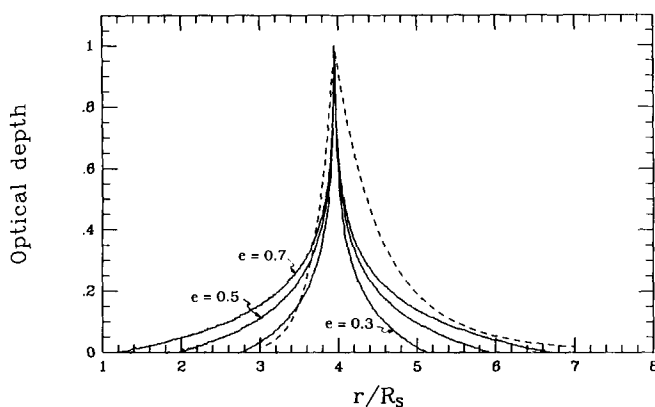


FIG. 4. The radial optical depth contribution of a single particle during a full period of its eccentricity oscillation for  $e_{\max} = 0.3, 0.5,$  and  $0.7$  (solid lines). These curves were constructed by first subtracting a constant value from the solution of Eq. (10) and then normalizing the peak at Enceladus' position to unity; this procedure is similar to the background sky subtraction performed on photographic plates. This normalization process causes the area under each curve to differ, but does preserve the symmetry around  $r = a$  in each case. Also plotted (dotted line) is the inferred radial brightness distribution based on the observations and represented by two power-law drop-offs from Enceladus (Showalter *et al.* 1991).

Runge–Kutta method, which we have tested by following a grain on its Kepler orbit about Saturn, neglecting all perturbations, for  $10^4$  years; in this simulation the particle's energy and angular momentum are maintained to accuracies of  $10^{-3}$ . In order to allow simpler interpretation of our results and more direct comparison with our idealized analytical model (4), we transform our numerical results from position  $\mathbf{r}$  and velocity  $\mathbf{v}$  into osculating orbital elements (Danby 1988).

Figure 5 shows the history of a  $1\text{-}\mu\text{m}$ -radius grain started on a circular orbit from Enceladus. The grain's eccentricity variation is seen to exhibit a nearly 10-year periodicity, driven by the orbit's precession. The grain's surface potential varies between  $-5.8$  and  $-5.4$  V, periodically changing from small to larger amplitude oscillations and closely imitating the eccentricity variations. The potential history reflects the radial dependence of the plasma parameters and, to a much lesser extent, the velocity modulation of the charging currents. The reader will observe from Fig. 1 that the insensitivity of  $\Phi$ 's dependence on position would not be true for  $\delta_M = 0$ . More importantly, Fig. 2 shows that a constant potential of  $-5.5$  V on a one-micrometer grain will produce a maximum eccentricity of nearly 0.7, in agreement with the second panel of Fig. 5. Note, however, that our numerical model does not include collisions with the inner rings and the displayed orbit attains a maximum eccentricity dangerously close to  $e'_{\text{coll}} \approx 0.65$ .

The orbital inclination  $i$ , always small, is maximum during periods when the eccentricity is large and when the Sun is far out of the ring plane. This behavior is a direct consequence of the pericenter locking described below (Hamilton and Burns 1992). Accordingly, there are two periodicities driving the inclination history of Fig. 5: that caused by the eccentricity variations with a period of  $\sim 10$  years set by the precession rate, and that caused by changes in the strength of the vertical force with a period of one-half Saturn's 29.5 year orbital period ( $\sim 15$  years). The maxima of these two oscillations line up every 30 years, which is the characteristic time between the largest inclinations ( $\sim 0.4^\circ$ ) observed in Fig. 5.

Finally, the out-of-plane radiation force causes  $\omega$  to lock at  $\pi/2$  when the Sun is above the ring plane and at  $-\pi/2$  when it is below the plane. Pericenter locking is only accomplished if  $\beta/e < (\dot{\omega}_{J_2} + \dot{\omega}_\Phi)$  (Hamilton and Burns 1992), i.e., when radiation pressure is *small* enough (note that the right-hand side of this expression, which involves time derivatives of the argument of pericenter rather than the longitude of pericenter, is not  $\gamma$  and is, in fact, usually large and positive). This somewhat counterintuitive result arises because locking only occurs for small inclinations; strong radiation pressure induces inclinations large enough to prevent the effect. When the pericenter is locked to  $\pm\pi/2$ , though, the orbit's ascending

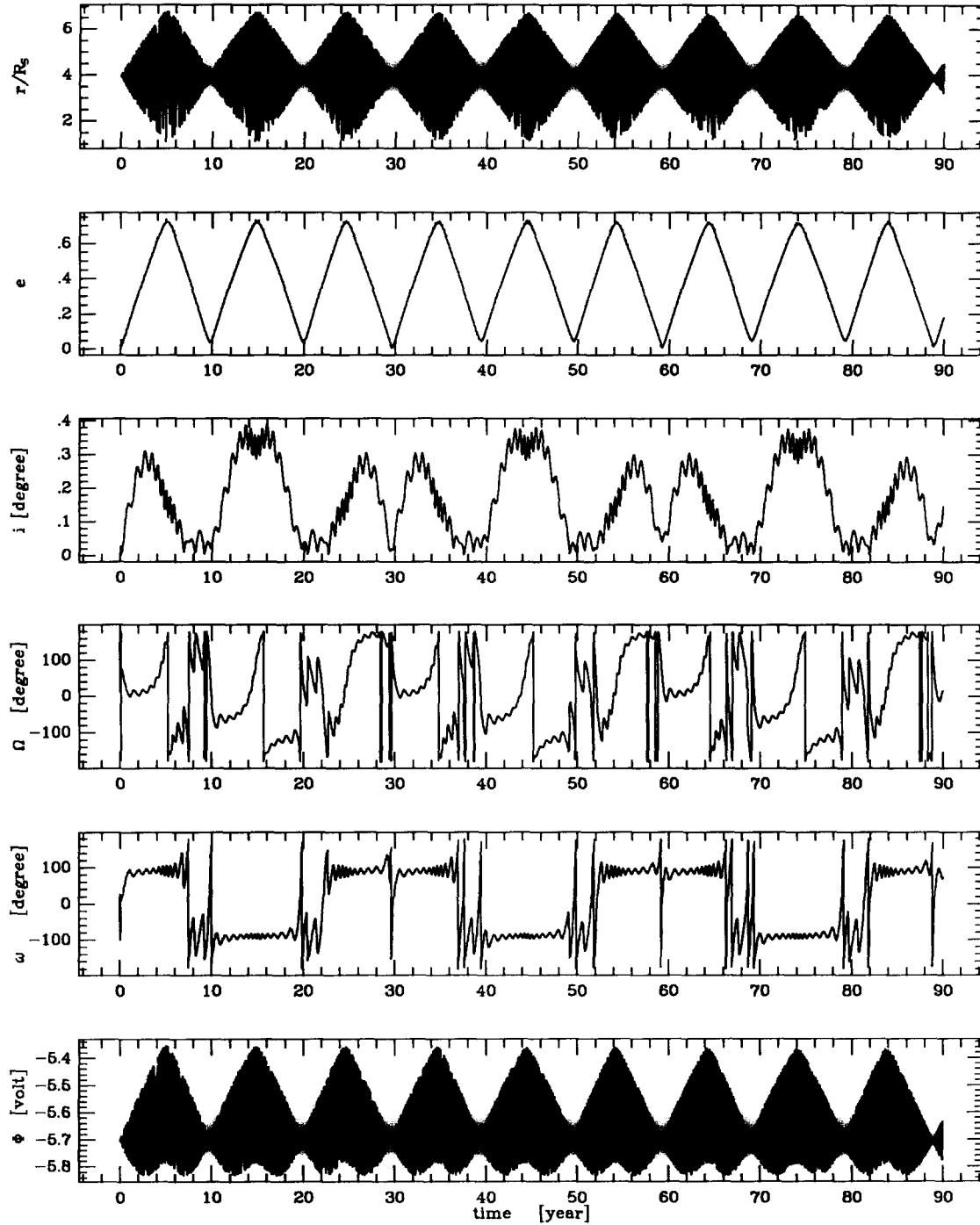


FIG. 5. The history of the orbital elements of a  $1\text{-}\mu\text{m}$  grain started from Enceladus on a circular orbit of radius  $a = 3.95R_S$ . The top panel shows  $r$ , the radial distance, which oscillates between the apocenter and pericenter distances  $a(1 + e)$  and  $a(1 - e)$ . The third panel displays the inclination  $i$ ,  $\Omega$  is the longitude of the ascending node and  $\omega$  is the argument of pericenter where  $\omega + \Omega \equiv \bar{\omega}$ ; as seen in the figure,  $\Omega$  and  $\omega$  become poorly constrained when  $i = 0$  and  $e = 0$ , respectively. The bottom panel shows the history of the surface potential  $\Phi$  which depends, in part, on the secondary yield parameters chosen ( $E_M = 500$  eV and  $\delta_M = 1.5$ , see Fig. 1).

and descending nodes lie along the latus rectum of the elliptical orbit. For locked orbits, therefore, the distance from Saturn to the orbital nodes is equal to the semilatus rectum which is given by  $a(1 - e^2)$ . Collisions with the

classical inner rings can only take place at one of these nodes since these rings are exceedingly thin (Cuzzi *et al.* 1979, Sicardy *et al.* 1982). Furthermore, since all other values of  $\omega$  cause one of the nodes to fall radially closer

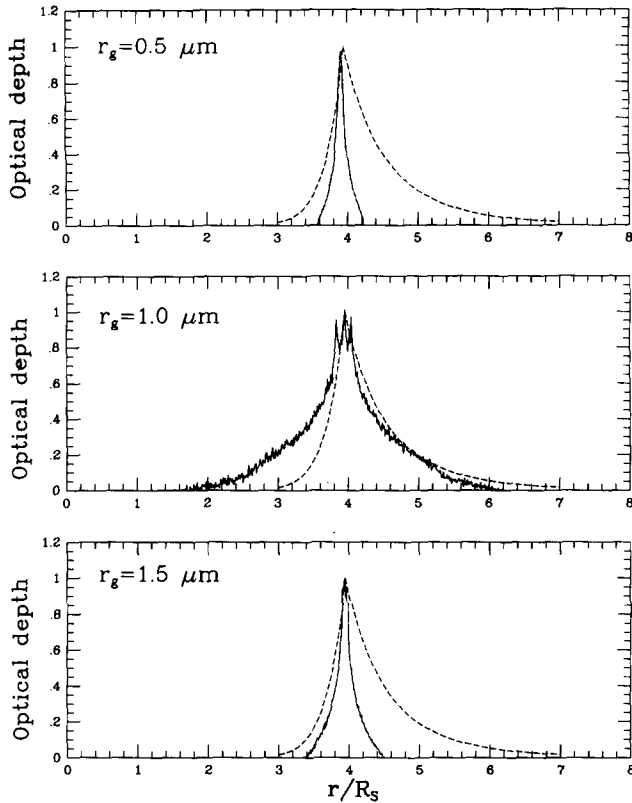


FIG. 6. The optical depth profiles (continuous lines) for grains of radii 0.5 (top), 1.0 (middle), and 1.5 (bottom) micrometers. All grains were given the same initial conditions as the one in Fig. 5, the orbits were sampled every 10 days for 90 years, and the curves were normalized as in Fig. 4. Also plotted for comparison are the Showalter *et al.* (1991) observations (dashed line). The plot clearly demonstrates the enhanced mobility enjoyed by the one micrometer-sized grains. The three maxima clustered near  $4R_S$  in the central panel are due to the fact that the grain's orbital eccentricity does not decrease to exactly zero on every cycle (see second panel of Fig. 5).

to the planet, the orbits under discussion are the least susceptible to collisions with the inner rings. Such orbits are very desirable when one is trying to spread material over a large radial range! A collision with the A ring is inevitable when  $a(1 - e^2) = 2.27R_S$  from which, for  $a = 3.95R_S$ ,  $e'_{\text{coll}} \approx 0.65$  (this result should be contrasted with the case of collision with the planet which occurs for  $a(1 - e''_{\text{coll}}) = 1$  or  $e''_{\text{coll}} \approx 0.75$ ).

In order to construct ring profiles, we followed grains of three sizes for 90 years (3 Saturn orbital periods) and noted their radial positions every 10 days. We then constructed radial optical depth profiles (Fig. 6) and scatter plots (Fig. 7) from the resulting orbits, normalizing the former in the same manner as in Fig. 4. The two figures show many of the characteristics of the observed ring (Showalter *et al.* 1991) and argue convincingly for a population of one-micrometer grains. As with our analytic result (plotted in Fig. 4), the optical depths

of the three simulated rings (Fig. 6) have a sharp peak near the source with a steep drop-off on either side. Only the one-micrometer grains, however, have an optical depth profile with a thickness anything like that of the actual ring. Similarly, the radial dependence of the ring thickness from our simulation for one-micrometer grains (Fig. 7) qualitatively imitates Showalter *et al.*'s (1991) interpretation of the Baum *et al.* (1981) ground-based observations described in the Introduction. Like the actual E ring, our model for solely one-micrometer grains has a greater thickness at its outer edge than close to the planet, and is thinnest at its source. Although the relative proportions are roughly correct, the magnitude of the predicted thickness is  $\sim 10$  times less than the observed thickness. Somewhat larger inclinations may be obtained by grains with slightly different sizes and charges or by a different plasma environment. These considerations alone, however, are probably unable to account for the observed maximum inclinations. The minimum in thickness that occurs near Enceladus' orbital radius (Fig. 7) can be explained by pericenter locking which, in addition to permitting the maximum  $e'_{\text{coll}}$  which allows the greatest radial spread, also forces

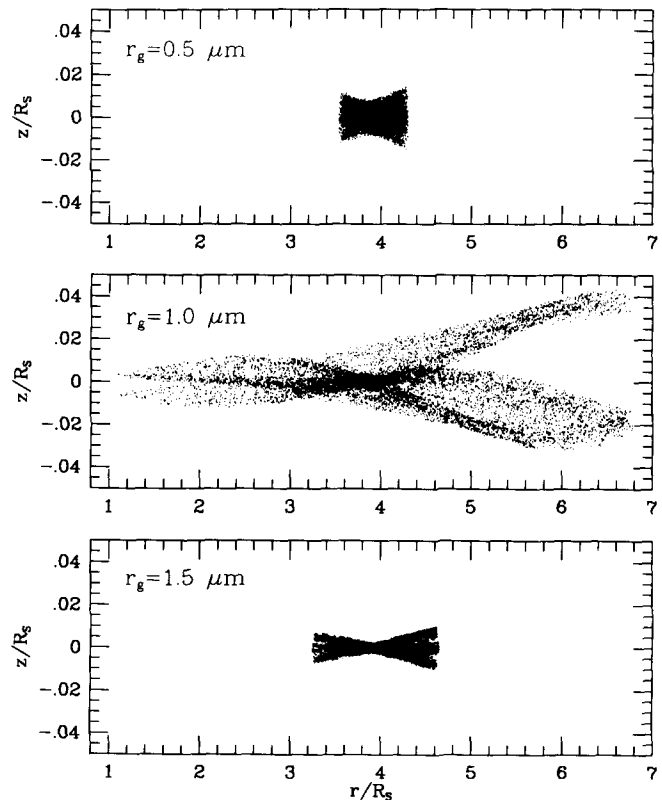


FIG. 7. A scatter diagram in the  $r = (x^2 + y^2)^{1/2}$ ,  $z$  plane for the orbits discussed in Fig. 6. The vertical structure for the one-micrometer grains is similar to the structure displayed by the actual E ring, although the heights attained in our simulations are a factor of  $\sim 10$  too small.

the nodes of the orbit to be radially close to that of the moon. By definition, vertical heights are minimum near orbital nodes.

The ring particles in our model are not distributed symmetrically in azimuth because, by (7) for the 2-D problem, the maximum eccentricity (for  $\gamma > 0$ ) is achieved when  $\tilde{\omega} = \pi$  (i.e., pericenter lies in the direction of the Sun). Our "model" ring thus bulges radially outward toward the Sun and is correspondingly compressed in the planet's shadow; these directions would be reversed if the particle size or charge were such that the orbital precession was in the opposite sense ( $\gamma < 0$ ). In reality, however, particles with both signs of  $\gamma$  are probably present which would cause the distribution to extend further toward and away from the Sun rather than in the perpendicular directions. As viewed from the Sun or, almost equivalently, the Earth, the model's radial distribution would appear less peaked at the source and less extended from that displayed in Fig. 6 and from that observed (Baum *et al.* 1981). Despite this, we have plotted an azimuthally averaged ring for reasons described later. Such a fore-aft bulge could not be identified in the available Voyager images (M. R. Showalter, private communication, 1991); inbound-outbound differences in Voyager plasma absorption detections, which have been interpreted as caused by an asymmetric E ring (Sittler *et al.* 1981), could not be due to the E ring studied here because our particles are too small and too widely separated to be effective absorbers.

#### FURTHER CONSIDERATION OF THE MODEL

We have demonstrated that a simple dynamical model does remarkably well at matching many features of the actual E ring. In this section we discuss the uncertainties in our model (particle sizes and magnetospheric parameters) and critically compare the results of our simulations with observable E ring features such as its asymmetry, density peak, and radial extent. We find that additional complications to the model seem capable of alleviating several discrepancies.

##### *Particle Sizes*

On the question of particle sizes, Showalter *et al.*'s (1991) photometric modeling, whose results we have adopted in this model, suggests that 1- $\mu\text{m}$  grains dominate both the forward- and back-scattered signals. In terms of the photometric data, macroscopic particles could provide at most a few tens of percent of the light; however, these larger particles could be radially localized without being discerned (M. R. Showalter, private communication, 1991). Following the rule that simplicity should be preferred over complexity, Showalter *et al.* (1991) did not test models with radially

variable distributions or odd size distributions against the available observations. Additional meaningful constraints can be placed on the mass of the E ring (Hood 1991), if one accepts that the observed low-energy electrons do not suffer significant absorptions by E ring particles. These constraints limit the overall contribution of macroscopic particles to the E ring's brightness to less than a percent. Within this framework, our assumption of solely 1- $\mu\text{m}$  particles seems acceptable.

Since our results for 1- $\mu\text{m}$  grains do so well at matching the observations, but seem to require what appears to be a finely tuned model, one might ask whether any processes favor micrometer-sized grains. This could occur if such grains are preferentially formed, or if they are better able to survive. Haff *et al.* (1983) and Pang *et al.* (1984) suggest that micrometer-sized grains alone may be produced by condensation as volcanoes or geysers on Enceladus jet into a vacuum, but such schemes seem contrived.

Are there any reasons why these small grains might survive longer than other-sized particles? Since lifetimes of small particles due to destruction vary as some function of particle size (Burns 1992), it does not seem feasible to generate a narrow particle size distribution by destructive means. On the other hand, it may be that micrometer-grains, due to their highly eccentric and inclined orbits, are less likely to suffer collisions. We have shown in Figs. 6 and 7 the distributions of 0.5, 1.0, and 1.5 micrometer-sized grains, all of which rely on the same dynamical and charging models as did Fig. 5. The fact that particles both larger and smaller than a micrometer remain so much more localized about their source can be simply understood from Fig. 2 where, for  $\Phi \approx -5.5$  V, much smaller  $e_{\text{max}}$ 's are achieved by 0.5- $\mu\text{m}$  and 1.5- $\mu\text{m}$  grains than by the observed 1.0- $\mu\text{m}$  particles. Grains on even slightly inclined orbits will have longer lifetimes against recollision than those that lie closely confined to the satellite's orbital plane. Since recollision determines lifetimes (see Burns *et al.* 1984), it is possible that, acting over time, the advantage that micrometer-sized grains have could yield a size distribution weighted toward that size.

##### *Magnetospheric Model*

The Richardson-Sittler (1990) magnetospheric model that we have taken for computing the particle's charge is based on limited observations obtained during the three spacecraft flybys of Saturn. Consequently, untested assumptions about time variability and azimuthal symmetry made necessary by the sparsity of the data set could cause predictions of the model to differ from actual conditions in the magnetosphere. Because our mechanism relies on a close match of the precession rates ( $\gamma$  small in Eq. (7a)),

it is possible that other plasma models would produce quite different dynamical histories for  $1.0\text{-}\mu\text{m}$  grains. Nevertheless, since the electromagnetic precession is size dependent while the gravitational one is not, there should always be some grain size for which  $\gamma$  is small; particles of these sizes will display orbital characteristics similar to those seen here.

#### *Azimuthal Asymmetry*

We suspect that the azimuthal asymmetry apparent in our model will not be present in a real ring driven by the processes that we have considered because the eccentricity history of a ring particle depends so sensitively on the grain's charge-to-mass ratio (see Fig. 2). There are two implications: (i) Even a relatively narrow size distribution centered at  $1\ \mu\text{m}$  is likely to have some particles for which  $\gamma > 0$  but others where  $\gamma < 0$  (this situation may be caused by slightly different grain radii, densities, or surface potentials, or by different average histories of charge); hence some particles will be preferentially found on the planet's side facing the Sun while others will congregate  $180^\circ$  away. (ii) The grain's predicted orbital history might also change on relatively brief time scales because the grain's potential may vary over time scales of an orbital period or shorter; such variations would occur as the particle moved into different plasma environments (e.g., due to the particle's radial motion [Burns and Schaffer 1989] or an asymmetric Saturnian plasmasphere like the Earth's), or as conditions changed throughout the entire magnetosphere. In these circumstances, the nature of our orbital solution will be fundamentally altered from that given by (7), which assumes grains to have started on circular paths. One can easily construct charging scenarios such that the preferred alignment set by (7b) is substantially weakened and that the maximum eccentricity is larger than that predicted by (7a).

#### *Semimajor Axis Shifts*

The characteristics of Saturn's E ring that we are attempting to match with our dynamical model include the radial asymmetry about Enceladus' orbit, the smeared peak of the E ring, and the full radial extent ( $3\text{--}8R_S$ ) of the ring. The match of our model to these features can be improved if some particles are allowed to attain semimajor axes that differ from that of Enceladus. Small shifts in an orbit's semimajor axis can occur in a number of ways.

In general, particles will be injected from Enceladus at slightly different radial distances because of the small underlying eccentricity (0.004) of that satellite's orbit and at slightly different velocities because, whatever the injection mechanism (e.g., geysers [Stevenson 1982, Haff *et al.* 1983, Pang *et al.* 1984] or meteoroid cratering [McKinnon 1983]), the particles will leave the satellite

with some, albeit relatively low, relative velocity. These two effects combine to allow slightly different ( $\approx 1\%$  change) starting semimajor axes. A wider spread in semimajor axes arises from changes in orbital energy that occur when an orbit passes through a planet's shadow, especially during edge-on configurations of the rings such as that present at the time of Baum *et al.*'s (1981) ground-based observations. Shadow passage produces a force component that varies with the orbital period, both due to a varying electric charge (as the photoemission current switches on and off, Horanyi and Burns 1991) as well as the lack of radiation pressure (Mignard 1984) in the shadowed regions. Both of these processes are capable of rapidly shifting the semimajor axes of orbits slightly inward or outward; the latter process can produce shifts of  $\pm 0.1R_S$  in less than a few years. Plasma drag and, under certain circumstances, resonant charge variations (Burns and Schaffer 1989, Northrop *et al.* 1989) will produce outward drifts over time scales of  $10^3\text{--}10^5$  years while neutral gas drag and Poynting–Robertson light drag cause inward drifts. These inward drags are believed to be less effective than the outward ones about Saturn (Burns 1992). Finally, temporal or spatial fluctuations in plasma properties will cause radial diffusion (Grün *et al.* 1984) of particle orbits.

Orbits shifted inward are preferentially lost by collisions with the inner rings simply because they are closer to the rings and, more significantly, because of a possible interaction with a strong Lorentz resonance located just interior to Enceladus at  $\approx 3.9R_S$  (Hamilton and Burns 1992). The latter resonant electromagnetic perturbation exists only if Saturn's highly symmetric magnetic field contains nonaxisymmetric terms. For example, a dipole tilt of only  $0.8^\circ$ , that initially proposed by Ness *et al.* (1982) (cf. Acuña *et al.* 1983), is sufficient to break the lock that requires the orbital nodes to remain near Enceladus' radial position. This will cause grains that have moved inward from Enceladus to be lost to the main rings much more rapidly (at much smaller eccentricities) than those drifting outward. In sum then, many of the above effects, in particular this Lorentz resonance, favor the retention of particles that have drifted outward from Enceladus.

#### *Embedded Satellites*

Besides Enceladus, the moons Mimas, Tethys, Dione, and the Lagrangian companions of the two latter satellites lie within the E ring. Satellite–ring interactions could take several forms. For example, gravity assists from close encounters could change a dust grain's orbital elements, most notably its semimajor axis. Simple estimates show that gravitational scattering from Enceladus can cause at

most a one percent change in the semimajor axis or induce inclinations of up to  $\approx 0.5^\circ$ . Scattering caused by the other moons is much less efficient since the relative velocities at which an E ring grain encounters these moons are very large. These other satellites, however, could possibly be additional sources for E ring material. Micrometeoroid collisions or impacts of E ring particles themselves into the moons could loft material off these small bodies. Micrometer-sized particles originating from nearby satellites will most likely have equilibrium potentials similar to that of grains from Enceladus (Fig. 1); hence, pericenter precession rates will match for particles similar in size to those considered here. As eccentricities grow and material spreads radially, these grains will merge with those emanating from Enceladus.

#### *Improvements to the Model*

The major shortcoming of our simple model is the fact that, in contrast to the actual ring, our ring's radial distribution is symmetric about the source satellite (see Fig. 6). This is due to the fact that the increased velocity as a particle heads inward along its eccentric orbit is exactly canceled by a decrease in the area contained in a radial hoop in the optical depth calculation. It is possible that the semimajor axis shifts discussed above cause the optical depth distribution to fall off more steeply inward than outward. Additional sources further out in the ring would also aid in explaining the asymmetry.

Furthermore, according to our simple model, material introduced at Enceladus can never reach the outer limits of the known E ring because, with the orbit's fixed semimajor axis (see Eq. 4a), any eccentric path that reaches beyond about  $6.5R_S$  would also penetrate the opaque inner rings. Semimajor axis shifts and especially outer satellite sources have the potential to overcome this shortcoming. The apparent outer boundary to the ring, which is most likely due to the weakening of signal relative to background, could also have dynamical causes. Grains may collide with Rhea and be lost from the ring (see below). Particles may only arrive at the largest radial distances if they are at the apocenters of highly elliptical orbits. Because of changes in the local plasma environment at  $8R_S$ , electric charges on particles that sample this region may be such that orbital precession is very rapid, in which case eccentricity growth by radiation pressure may cease. The inner boundary at about  $3R_S$  may be caused by collisions with Mimas and the G ring or may be an artifact of the image processing and interpretation, which is difficult to carry out near the bright glare of the main rings.

Finally, although our model of material originating from Enceladus successfully (and not surprisingly) indicates that the ring's optical depth will be maximum at Encela-

cus, it predicts an unusual triple peak near Enceladus (Fig. 6). The peak is easily smeared by summing over a distribution of particles launched under slightly different conditions (launch positions and velocities, season, particle sizes, etc.). In addition, many other processes, including the semimajor axis shifts discussed above, will act to further soften any sharp feature.

#### CONSEQUENCES AND CONCLUSIONS

The process of eccentricity-pumping that we have invoked here to account for the global distribution of the E ring may produce other noticeable consequences in the Saturnian system. Some E ring particles will strike the main ring system. Such impacts will kick up some  $10^3$ – $10^4$  times their mass in micrometer-sized ejecta (Burns *et al.* 1984). Crudely, such material would account for an optical depth of at most  $10^{-3}$ , not much but possibly measurable since the main rings contain so little dust (Doyle *et al.*, 1989).

Since radial spreading of injected grains occurs very rapidly according to the dynamics discussed here, there is the possibility of episodic brightness variations in the E ring if Enceladus abruptly injects dust into the system, whether through geysers or meteoroid impacts. It will take somewhat longer for the particles to be dispersed latitudinally but even then this distribution will occur after only half a Saturnian orbit period, or about 15 years.

If Enceladus is the source of the E ring and particles are swiftly driven onto eccentric paths, satellites interior and exterior to Enceladus should be systematically struck by this material. Particles at the apocenters of moderately eccentric orbits will suffer high-speed impacts onto the leading faces of the satellites Dione, Tethys, and Rhea that also pass through this region: collisional lifetimes are short, of order 100 years or less (cf. Burns *et al.* 1984). Interestingly, the leading sides of these satellites have higher albedos and are photometrically bland, perhaps owing to enhanced meteoroid erosion of their front faces (Clark *et al.* 1986, Veverka *et al.* 1986, Buratti *et al.* 1990). Ring particles at their pericenters will be moving faster than the innermost classical moon Mimas and will strike its trailing side for which a similar leading/trailing dichotomy is visible in the satellite's photometric properties (Verbiscer and Veverka 1992).

We are encouraged by the success of this simple model. But even if it turns out that the life cycle of E ring grains is determined by other processes, such as condensation from the local plasma (Johnson *et al.* 1989, Morfill *et al.* 1992) or more leisurely orbital evolution due to magnetospheric interactions alone (Havnes *et al.* 1992), we have demonstrated that investigations of these other mechanisms must assume that the E ring particles move along

moderately noncircular orbits because such paths are inevitable for charged, micrometer-sized grains looping about Saturn.

#### ACKNOWLEDGMENTS

We thank L. L. Hood for discussions, as well as O. Havnes and an anonymous reviewer for constructive suggestions. This work was supported by NASA Grants NAGW-310 and NAGW-1914. JAB expresses his appreciation to Peter Gierasch for overseeing the paper's review.

#### REFERENCES

- ACUÑA, M. H., J. E. P. CONNERNEY, AND N. F. NESS 1983. The  $Z_3$  zonal harmonic model of Saturn's magnetic field: Analyses and implications. *J. Geophys. Res.* **88**, 8771–8778.
- BAUM, W. A., T. KREIDL, J. A. WESTPHAL, G. E. DANIELSON, P. K. SEIDELMANN, D. PASCU, AND D. G. CURRIE 1981. Saturn's E ring. I. CCD observations of March 1980. *Icarus* **47**, 484–496.
- BURATTI, B. J., J. A. MOSHER, AND T. V. JOHNSON 1990. Albedo and color maps of the Saturnian satellites. *Icarus* **87**, 339–357.
- BURNS, J. A. 1992. Physical processes on circumplanetary dust. In *Origin and Evolution of Interplanetary Dust* (A.-C. Levasseur-Regourd and H. Hasegawa, Eds.). Kluwer, Dordrecht, in press.
- BURNS, J. A., P. L. LAMY, AND S. SOTER 1979. Radiation forces on small particles in the solar system. *Icarus* **40**, 1–48.
- BURNS, J. A., AND L. E. SCHAFFER 1989. Orbital evolution of circumplanetary dust by resonant charge variations. *Nature* **337**, 340–343.
- BURNS, J. A., M. R. SHOWALTER, AND G. E. MORFILL 1984. The ethereal rings of Jupiter and Saturn. In *Planetary Rings* (R. Greenberg and A. Brahic, Eds.), pp. 200–272. Univ. of Arizona Press, Tucson.
- CHAMBERLAIN, J. W. 1979. Depletion of satellite atoms in a collisionless exosphere by radiation pressure. *Icarus* **39**, 286–294.
- CLARK, R. N., F. P. FANALE, AND M. GAFFEY 1986. Surface composition of natural satellites. In *Satellites* (J. A. Burns and M. S. Matthews, Eds.), pp. 437–491. Univ. of Arizona Press, Tucson.
- CUZZI, J. N., J. A. BURNS, R. H. DURISEN, AND P. HAMILL 1979. The vertical structure and thickness of Saturn's rings. *Nature* **281**, 202–204.
- DANBY, J. M. A. 1988. *Celestial Mechanics*, 2nd ed. Willmann-Bell Richmond, VA.
- DOYLE, L. R., L. DONES, AND J. N. CUZZI 1989. Radiative transfer modelling of Saturn's outer B ring. *Icarus* **80**, 104–135.
- DRAINE, B. T., AND E. E. SALPETER 1979. On the physics of dust grains in hot gas. *Astrophys. J.* **231**, 77–94.
- GRÜN, E., G. E. MORFILL, AND D. A. MENDIS 1984. Dust-magnetosphere interactions. In *Planetary Rings* (R. Greenberg and A. Brahic, Eds.), pp. 275–332. Univ. of Arizona Press, Tucson.
- HAFF, P. K., A. EVIATAR, AND G. L. SISCOE 1983. Ring and plasma: The enigma of Enceladus. *Icarus* **56**, 426–438.
- HAMILTON, D. P., AND J. A. BURNS 1992. Motion of a small grain in a planetary magnetosphere: Orbit-averaged perturbation equations for electromagnetic and radiation forces. Manuscript in preparation.
- HAVNES, O., G. E. MORFILL, AND F. MELANDSØ 1992. Orbit evolution of dust in planetary magnetospheres. *Icarus* (in press).
- HOOD, L. L. 1991. Constraints on physical properties of Saturn's G and E rings from energetic charged particle measurements. Submitted for publication.
- HORANYI, M., AND J. A. BURNS 1991. Charged dust dynamics: Orbital resonance due to planetary shadows. *J. Geophys. Res.* **96**, 19283–19289.
- HORANYI, M., J. A. BURNS, M. TATRALLYAY, AND J. G. LUHMANN 1990. Toward understanding the fate of dust lost from the Martian satellites. *Geophys. Res. Lett.* **17**, 853–856.
- HORANYI, M., H. L. F. HOUPIS, AND D. A. MENDIS 1988. Charged dust in the Earth's magnetosphere: Physical and dynamical processes. *Astrophys. Space Sci.* **144**, 215–229.
- HORANYI, M., AND D. A. MENDIS 1987. The effect of sector boundary crossing on the cometary dust tail. *Earth Moon Planets* **37**, 71–77.
- JOHNSON, R. E., M. K. POSPIESZALSKA, E. C. SITTLER, JR., A. F. CHENG, L. J. LANZEROTTI, AND E. M. SIEVEKA 1989. The neutral cloud and heavy ion inner torus at Saturn. *Icarus* **77**, 311–329.
- McKINNON, W. B. 1983. Origin of E ring: Condensation of impact vapor . . . or boiling of impact melt. *Lunar Planet. Sci. XIV*, 487–488.
- MIGNARD, F. 1984. Effects of radiation forces on dust particles in planetary rings. In *Planetary Rings* (R. Greenberg and A. Brahic, Eds.), pp. 333–366. Univ. of Arizona Press, Tucson.
- MORFILL, G. E., O. HAVNES, AND C. K. GOERTZ 1992. Submitted for publication.
- NESS, N. F., M. H. ACUÑA, K. W. BEHANNON, L. F. BURLAGA, J. E. P. CONNERNEY, AND R. P. LEPPING 1982. Magnetic field studies by Voyager 2: Preliminary results at Saturn. *Science* **215**, 558–563.
- NORTHROP, T. G., D. A. MENDIS, AND L. SCHAFFER 1989. Gyrophase drifts and the orbital evolution of dust at Jupiter's gossamer ring. *Icarus* **79**, 101–115.
- PANG, K. D., C. C. VOGEL, AND J. W. RHOADS 1984. Macrostructure and microphysics of Saturn's E ring. In *Anneaux des Planetes* (A. Brahic, Ed.), pp. 607–613. Cepaude, Toulouse.
- RICHARDSON, J. D., AND E. C. SITTLER, JR. 1990. A plasma density model for Saturn based on Voyager observations. *J. Geophys. Res.* **95**, 12019–12120.
- SCHAFFER, L., AND J. A. BURNS 1987. The dynamics of weakly charged dust: Motion through Jupiter's gravitational and magnetic fields. *J. Geophys. Res.* **92**, 2264–2280.
- SCHAFFER, L., AND J. A. BURNS 1992. Stochastic charging of dust grains and its effects on Lorentz resonances in planetary rings. *J. Geophys. Res.*, in press.
- SHOWALTER, M. R., J. N. CUZZI, AND S. M. LARSON 1991. Structure and particle properties of Saturn's E ring. *Icarus* **94**, 451–473.
- SICARDY, B., J. LECACHEUX, P. LAQUES, R. DESPIAU, AND A. AUGE 1982. Apparent thickness and scattering properties of Saturn's rings from March 1980 observations. *Astron. Astrophys.* **108**, 296–305.
- SITTLER, E. C., JR., J. D. SCUDDER, AND H. S. BRIDGE 1981. Detection of the distribution of neutral gas and dust in the vicinity of Saturn. *Nature* **292**, 711–713.
- STEVENSON, D. J. 1982. Volcanism and igneous processes in small icy satellites. *Nature* **298**, 142–144.
- SUSZCZYNSKY, D. M., J. E. BOROVSKY, AND C. K. GOERTZ 1992. Secondary electron yields of Solar System ices. *J. Geophys. Res.* **97**, 2611–2619.
- VERBISCHER, A., AND J. VEVERKA 1992. Mimas: Photometric roughness and albedo map. *Icarus*, in press.
- VEVERKA, J., P. THOMAS, T. V. JOHNSON, D. MATSON, AND K. HOUSEN 1986. The physical characteristics of satellite surfaces. In *Satellites* (J. A. Burns and M. S. Matthews, Eds.), pp. 342–402. Univ. of Arizona Press, Tucson.
- WHIPPLE, E. C. 1981. Potential of surfaces in space. *Rep. Prog. Phys.* **44**, 1197–1250.
- WILLIS, R. F., M. ANDEREGG, B. FEUERBACHER, AND B. FITTON 1973. Photoemission and secondary electron emission from lunar surface material. In *Photon and Particle Interactions with Surfaces in Space* (R. J. L. Gard, Ed.), pp. 389–401. Reidel, Boston.